Revision 3: Phase Transformation of Hydrous Ringwoodite to the Lower-Mantle Phases and the Formation of Dense Hydrous Silica

Huawei Chen[1], Kurt Leinenweber[2], Vitali Prakapenka[3], Martin Kunz[4], Hans A. Bechtel[4], Zhenxian Liu[5] and Sang-Heon Shim[1]

[1]School of Earth and Space Exploration, Arizona State University, Tempe, Arizona.

[2]Eyring Materials Center, Arizona State University, Tempe, Arizona.

[3]GeoSoilEnviroCars, University of Chicago, Chicago, Illinois.

[4]Advanced Light Source Division, Lawrence Berkeley National Laboratory, Berkeley, California.

[5]Geophysical Laboratory, Carnegie Institution of Washington, Washington, DC.

Keywords: stishovite, ringwoodite, bridgmanite, periclase, water, mantle

Abstract

In order to understand the effects of H_2O on the mineral phases forming under the pressure-temperature conditions of the lower mantle, we have conducted laser-heated diamond-anvil cell experiments on hydrous ringwoodite (Mg_2SiO_4 with 1.1wt% H_2O) at pressures between 29 and 59 GPa and temperatures between 1200 and 2400 K. Our experimental results show that hydrous ringwoodite (hRw) converts to crystalline dense hydrous silica, stishovite (Stv) or $CaCl_2$-type SiO_2 (mStv), containing 1 wt% H_2O together with Brd and MgO at the pressure-temperature conditions expected for shallow lower-mantle depths between approximately 660 to 1600 km. Considering lack of sign for melting in our experiments, our preferred interpretation of the observation is that Brd partially breaks down to dense hydrous silica and periclase (Pc), forming Brd + Pc + Stv mineralogy. Our experiments may provide an explanation for the enigmatic coexistence of Stv and Fp inclusions in lower-mantle diamonds.

Introduction

Lines of evidence support that the lower mantle has a similar chemical composition to the upper mantle (Kurnosov et al., 2017; Shim et al., 2001a, 2017) that is likely peridotitic or pyrolitic (McDonough and Sun, 1995). In a pyrolitic lower mantle, $(Mg,Fe)(Al,Si)O_3$ bridgmanite (Brd) and (Mg,Fe)O ferropericlase (Fp) are the dominant minerals (Kesson et al., 1998; Lee et al., 2004). The high Mg/Si ratio of pyrolite stabilizes (Mg,Fe)O as a mineral phase (Fp) in the lower mantle. Fp would react with a free silica phase and forms Brd: (Mg,Fe)O (Fp) + SiO_2 = $(Mg,Fe)SiO_3$ (Brd). Therefore, it is believed that dense silica phases, such as stishovite (Stv), are not thermodynamically stable in the anhydrous lower mantle (Shim et al., 2001a).

In contrast, numerous studies have documented Stv coexisting with (Mg,Fe)O and Brd (pyroxene with a Brd-like composition) as inclusions in diamonds from the lower mantle (Kaminsky, 2012; Litvin et al., 2014; Stachel et al., 2005). Because the pyrolite model cannot explain the co-existence of Stv and (Mg,Fe)O, the diamond inclusions raise an important question about the mineralogy and composition of the lower mantle (Kaminsky, 2012). Alternatively, the inclusions may originate from non-pyrolitic sources. For example, Stv can exist with (Mg,Fe)O in a system with a much higher Fe content than pyrolite (Fei et al., 1996). However, many of the (Mg,Fe)O inclusions do not have sufficient Fe for this scenario, and so Brd should be observed instead of Stv in those cases. Experiments have shown that subducted basalt contains Stv together with Brd but not with Fp at the lower-mantle pressure–temperature (*P*–*T*) conditions (Hirose et al., 2005). Therefore, this cannot explain diamond inclusion observations.

An important factor to consider is the possible presence of H_2O. Studies have shown that minerals in the mantle transition zone can store H_2O up to a few wt% (Smyth 1994; Hirschmann 2006; Pearson et al. 2014). Indeed, some diamond inclusions indicated the premise that the mantle transition zone is hydrated at least locally (Pearson et al., 2014; Tschauner et al., 2018). However, recent high-pressure experiments have shown very low H_2O storage capacities for Brd and Fp in the lower mantle (Bolfan-Casanova et al. 2003; Panero et al. 2015). Therefore, H_2O transport via mantle convection across such a dramatic change in the H_2O storage capacity at 660-km depth can induce some important changes in the mineralogy of the lower mantle (Schmandt et al., 2014; Tschauner et al., 2018). To understand the effect of H_2O on lower-mantle mineralogy, we have conducted laser-heated diamond-anvil cell (LHDAC) experiments on a synthetic hydrous ringwoodite (Mg_2SiO_4 with 1.1wt% H_2O; hRw) starting material at pressures between 29 and 59 GPa and temperatures between 1200 and 2400 K, which is expected for the lower mantle.

Experimental Methods

Starting material: We synthesized Mg_2SiO_4 ringwoodite (Rw) from a molar mixture ($0.613Mg_2SiO_4 + 0.084SiO_2 + 0.167Mg(OH)_2$) from forsterite, SiO_2 (glass), and brucite for synthesis of a Mg_2SiO_4 with 3 wt% H_2O in a 6-8 multi-anvil press combined with a 10/5 assemblies at Arizona State University (ASU) (Leinenweber et al., 2012). The starting mixture was loaded into a platinum capsule. Then, we sealed the capsule. We compressed the mixture to 20 GPa and subsequently heated to 1573 K for 30 minutes. After the synthesis, pure ringwoodite was confirmed by X-ray diffraction (XRD) pattern (Fig. S1), which we will describe later. From analysis of infrared (IR) spectra, we obtained 1.1±0.5 wt% H_2O for the amount of H_2O in Rw from integrated intensity of the O-H vibration mode from infrared at the wavenumber 2600-3600 cm^{-1} range, following the methods in Smyth et al. (2003) (Fig. S2).

Laser-heated diamond-anvil cell: We pre-compressed the powder of the hydrous Rw sample into a 10-μm thick foil into a symmetric diamond anvil cell (DAC). We used diamond anvils with 200 μm (flat) and 150 μm (single beveled) cullets for experiments at pressures below and above 50 GPa, respectively. The sample chamber was made by drilling a 90 or 120 μm diameter hole in a rhenium gasket indented by diamond anvils. Two different types of heating were performed using either Ar or Ne as an insulating medium. The first was CO_2 laser heating on the hydrous Rw samples, and the second near infrared (NIR) laser heating (Fig. S3) on hydrous Rw + Pt mixtures (Tab. 1). For the CO_2 laser heating experiments, we cryogenically loaded an Ar medium in a DAC. A ruby chip was loaded at the edge of the sample chamber for pressure measurements, but away from the sample foil in order to avoid any chemical reaction. We compressed the samples with nitrogen-free type-II diamond anvils and focused a CO_2 laser beam on the sample foil in the DAC. Single-sided heating was conducted at 1200 to 2420 K using a laser heating system at ASU. Note that we did not mix the ringwoodite powder with any metals in the CO_2 heating experiments, because silicate samples couple directly with the CO_2 laser beam. The size of the laser heating spot was 50 μm. Temperatures were calculated by fitting the measured thermal radiation spectra to the Planck equation from one side of the sample after subtracting the backgrounds from the optics in the system similar to the method described in (Prakapenka et al., 2008). Pressure was measured using the ruby fluorescence line shift or the first-order Raman mode from the tips of the diamond anvils (Mao et al., 1978). For the NIR measurements, we mixed the Rw starting material with 10 wt% Pt, the latter being used as a laser coupler and internal pressure standard when using XRD (Ye et al. 2017). We loaded Ne as a pressure medium using the gas-loading system at the GESCARS, APS. The NIR laser heating was conducted at GSECARS (Prakapenka et al., 2008). Two near-infrared laser beams (~1 micron wavelength) were focused on the sample through two opposite sides of DAC with a hot spot size of 20–25 μm in diameter. The laser beams were aligned co-axially with the X-ray beam. Temperatures were calculated by fitting thermal radiation spectra to the Planck equation from both sides of the sample after background subtraction.

Synchrotron X-ray diffraction: We conducted synchrotron X-ray diffraction (XRD) experiments at beamlines 13IDD at APS and 12.2.2 at ALS (Kunz et al., 2005; Prakapenka et al., 2008). For the samples heated with a CO_2 laser beam at ASU, we conducted the measurements at high pressure and 300 K. In the case of the NIR heating, we conducted XRD measurements during laser heating at the beamline (see supplementary information). Pressure was calculated from the equations state of Ar and Pt for the CO_2 and NIR laser heated samples, respectively (Ross et al., 1986; Ye et al., 2017). The heating durations were 15–30 minutes. We collected diffraction patterns from a monochromatic X-ray beam with a wavelength of either 0.3344, 0.4133, or 0.4959 Å. The sizes of the X-ray focus at the sample were 3×4 and 10×10 μm^2 at beamlines 13IDD and 12.2.2, respectively. Diffraction patterns were measured with MarCCD and Pilatus detectors at beamlines 12.2.2 and 13IDD, respectively, with a detector distance of approximately 250 mm. We integrated the diffraction images to 1D patterns in the Dioptas package shown in Fig. S4 (Prescher and Prakapenka, 2015). We performed phase identification and peak fitting in the PeakPo package (Shim 2017). The data obtained from the GSECARS and the 12.2.2 beamlines agreed well with each other. Rietveld refinements were performed using the GSAS-II package (Toby and Von Dreele, 2013) (Table 2 and Fig. S5). We refined phase fractions first, then atomic positions, lattice parameters and spherical harmonic terms for the preferred orientation. After reaching a good visual fit, we refined all the parameters together to further reduce residuals after background subtraction, $R_{\text{wp-bknd}}$. From the unit-cell volume, we calculated the water content using the relationship presented in Nisr et al. (2017a) (Table 1).

Infrared spectroscopy: We conducted IR measurements on polycrystalline hydrous Rw starting material and the recovered samples at beamlines 1.4 of ALS and U2A of NSLS. We loaded the sample of ringwoodite in the sample chamber of the rhenium gasket in the diamond anvil cell. The infrared beam was focused on the sample to the minimum beamsize of 10×10 μm. We measure the infrared spectra of the sample at 1 bar. For hydrous stishovite, we measure the IR after laser heating of the hydrous ringwoodite sample. At ALS, the system consists of a Nicolet Magna 760 FTIR spectrometer and custom IR microscope with a HgCdTe detector and KBr beamsplitter. At U2A, we used a Bruker Vertex 80v FTIR spectrometer and Hyperion 2000 microscope with HgCdTe detectors. Spectral resolution was 4 cm^{-1}. Spectra were recorded for 256 scans. The beam-size was 10×10 μm^2 in diameter at the sample. We conducted spectral fitting for the IR data using the LMFIT package (Newville et al. 2014).

Results

Ringwoodite has a Mg/Si ratio of ~2. Thus, heating converts Rw to Brd ($MgSiO_3$) and MgO (periclase, Pc) without silica at the *P*–*T* conditions expected for the lower mantle (Shim et al., 2001a). All the diffraction patterns we measured after CO_2 laser heating between 35 and 55 GPa, however, showed the peaks of silica (either Stv or its orthorhombic modification in $CaCl_2$-type structure, mStv, together with those of Brd and MgO (Fig. 1). The most intense diffraction line of Stv (and mStv) exists at 2.8–2.9 Å. Because Brd and MgO do not have diffraction lines in this range, the appearance of the intense silica line allows us to unambiguously identify Stv (or mStv). In addition, some high-angle lines of Stv or mStv were identified, such as 101, 211, and 220. However, those features are less unambiguously as diagnostic features because of possible overlaps with the Brd and MgO lines. We also found Stv (or mStv) together with Brd and MgO in the NIR heating experiments (Fig. S3). CO_2 laser heating provides much larger heating spot and therefore low thermal gradients. Most importantly, hydrous Rw couples directly with a CO_2 laser beam. Because of these reasons, we discuss the CO_2 heating results in this paper (note that the NIR heating results are provided in supplementary information).

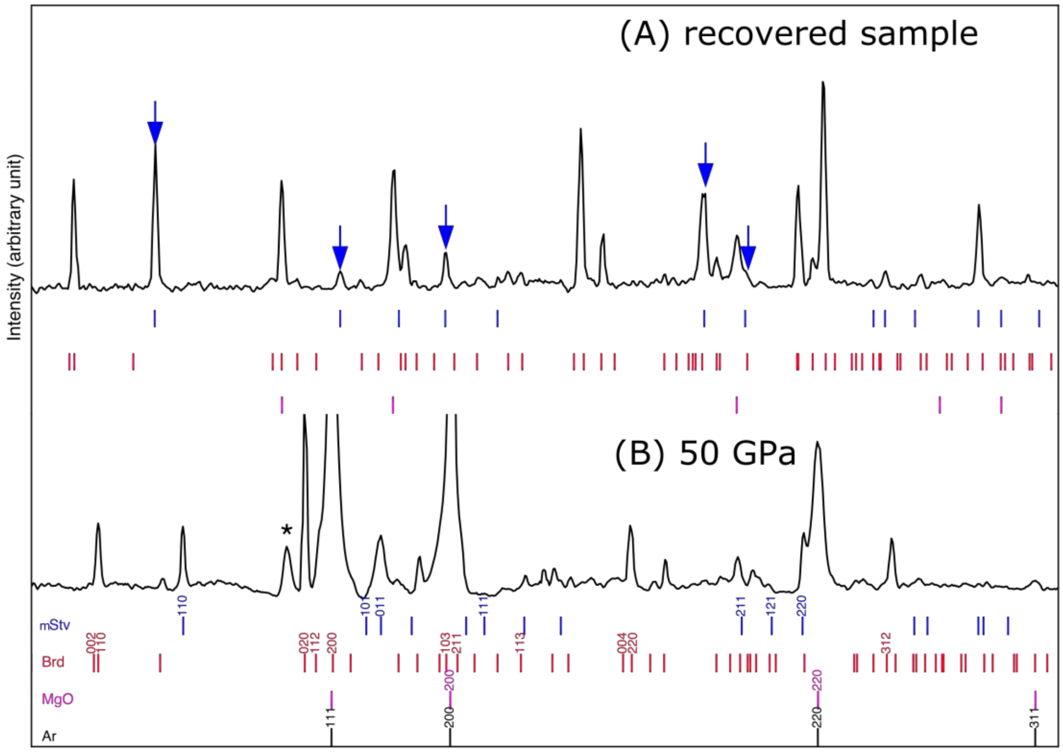

Fig. 1. X-ray diffraction patterns of lower-mantle minerals transformed from hydrous ringwoodite. a, 1 bar after recovery (X-ray wavelength of 0.3344 Å). b, 50 GPa after heating at 1200 K. The colored ticks below the patterns indicate the expected peak positions (Brd: bridgmanite, Pc: periclase (MgO), Stv: stishovite, Ct-SiO_2: $CaCl_2$-type silica (or mStv), Ar: argon, *: hcp-Ar). The blue arrows highlight the peaks from Stv (or converted from mStv). The Miller indices are provided for the lines with significant intensities (10%).

We have successfully quenched most of the samples synthesized at 35–55 GPa and measured their diffraction patterns at 1 bar (Fig. 1). All three phases observed at high pressure, Stv, Brd, and MgO, remained present after the pressure quench. The diffraction lines of silica were indexed well with the tetragonal rutile type, that is Stv. The unit-cell volumes of Brd and MgO at 1 bar were in agreement with their anhydrous counterparts within 1.0%. However, for Stv, we found much larger unit-cell volumes than the value reported for anhydrous Stv by 1.7–5.2% in Table 2.

Incorporation of H_2O increases the unit-cell volume of Stv and the relationship between the H_2O content and the volume expansion was measured quantitatively (Spektor et al. 2011, 2016; Nisr et al. 2017a). From the volume and H_2O content relationship found in other studies (Nisr et al., 2017; Spektor et al., 2016), we obtained 0.4–1.3 wt% H_2O for the recovered Stv. In Nisr et al. (2017a), the relationship between the H_2O content and unit-cell volume of stishovite was fit to a line using the samples from Spektor et al. (2016): water content (wt%) = $4.64 \pm 0.57 \times (V - 46.515)$, where V is the unit-cell volume. The H_2O contents of all the samples used for the calibration were directly measured from thermogravimetric analysis (TGA). Some of these samples were also characterized with IR measurements.

Stishovite has a tetragonal unit cell with two independent lattice parameters, *a* and *c*. When Stv is hydrated, the *a*-axis expands while the *c*-axis remains essentially unchanged. Such changes could be related to the bonding of hydrogen to the underbonded oxygen in the silicon defects in the crystal structure (Nisr et al., 2017; Spektor et al., 2011). We found a strong linear correlation between the c/a ratio and the unit-cell volume of the recovered Stv (Fig. 3a and Table 2). The trend in our dataset is in agreement with that found in previous studies on hydrous Stv (Spektor et al., 2016, 2011).

Infrared (IR) spectroscopy is sensitive to even a trace amount of hydroxyl incorporated in the crystal structures of mineral phases (Rossman, 1996). We measured the IR spectra of the samples recovered from the CO_2 lasers where we found complete conversion to the lower-mantle mineral phases, and did not find any Rw diffraction peaks after heating. We found multiples of OH vibrational modes from the recovered samples (Fig. 2b). The detected modes are significantly different from those of hRw (our starting material), MgO, and Brd in both wavenumber and intensity distribution (Bolfan-Casanova et al. 2002, 2003; Pearson et al. 2014; Panero et al. 2015). H_2O can significantly reduce the transition pressure of Stv to its orthorhombic modification (the $CaCl_2$ type, mStv), for example from 55 GPa to 25 GPa by 3 wt% H_2O (Lakshtanov et al. 2007; Nisr et al. 2017b). However, the differences in diffraction pattern between the phases are subtle, particularly if the incorporated H_2O contents are low. In some diffraction patterns, we were able to identify some diagnostic features of the orthorhombic distortion related to the broadening of stishovite 101 peak as suggested in Fig. 1. However, the severe peak overlaps of the Stv or mStv diffraction lines with Brd, MgO, and Ar at *d*-spacings smaller than 2.5 Å, made the unambiguous detection challenging. Therefore, we cannot rule out the possibility of a $CaCl_2$-type distortion in the silica phase (mStv) in our pressure range.

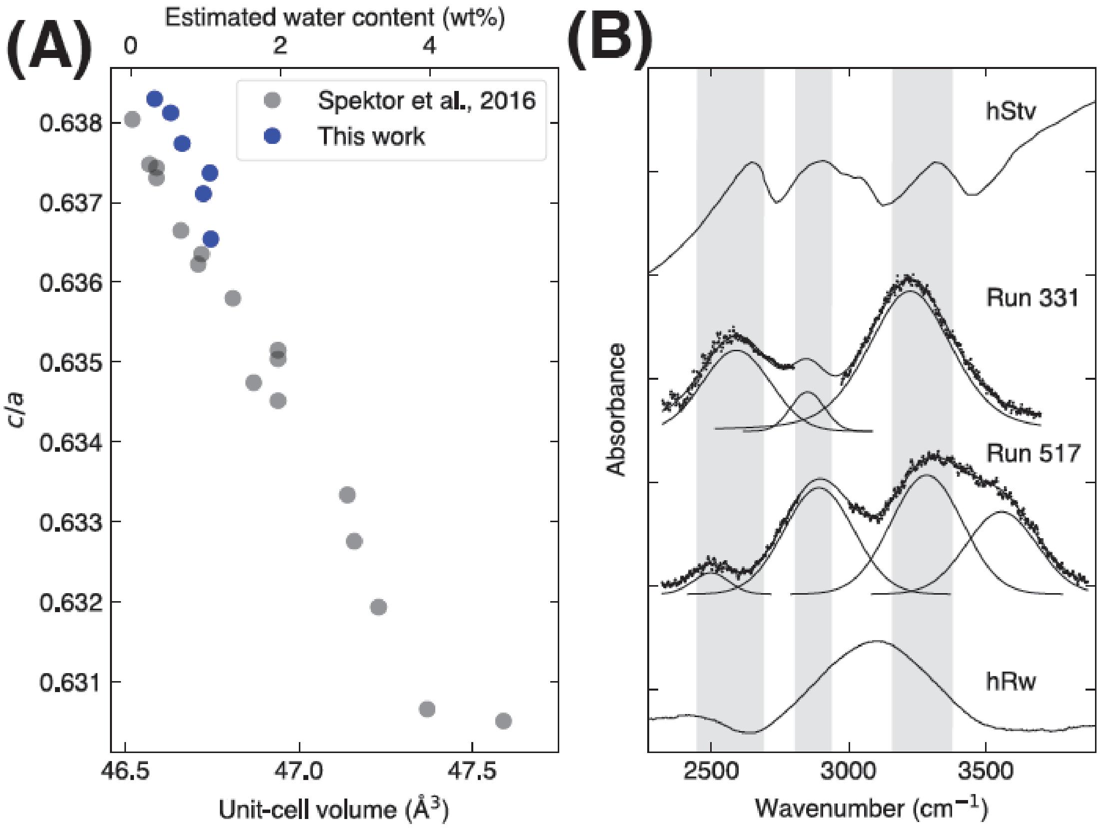

Fig. 2. The solubility of H_2O in Stv (or mStv) and its effects on the lower-mantle mineralogy. a, The *c*/*a* ratio and the unit-cell volume of the recovered Stv co-existing with Brd and MgO. For comparison, we plot the data for hydrous Stv (Spektor et al., 2016). b, The IR spectra of the samples recovered from the CO_2 heating experiments (dots) with spectral fitting results (black curves). We also present the IR spectra of the starting material (hydrous Rw) and hydrous Stv (Spektor et al., 2011). The gap at 2800–3000 cm^{-1} is a region for C-H modes from CH contaminants on diamond anvils. After opening the diamond-anvil cell, we measured IR through one diamond anvil to prevent accidental loss of the sample.

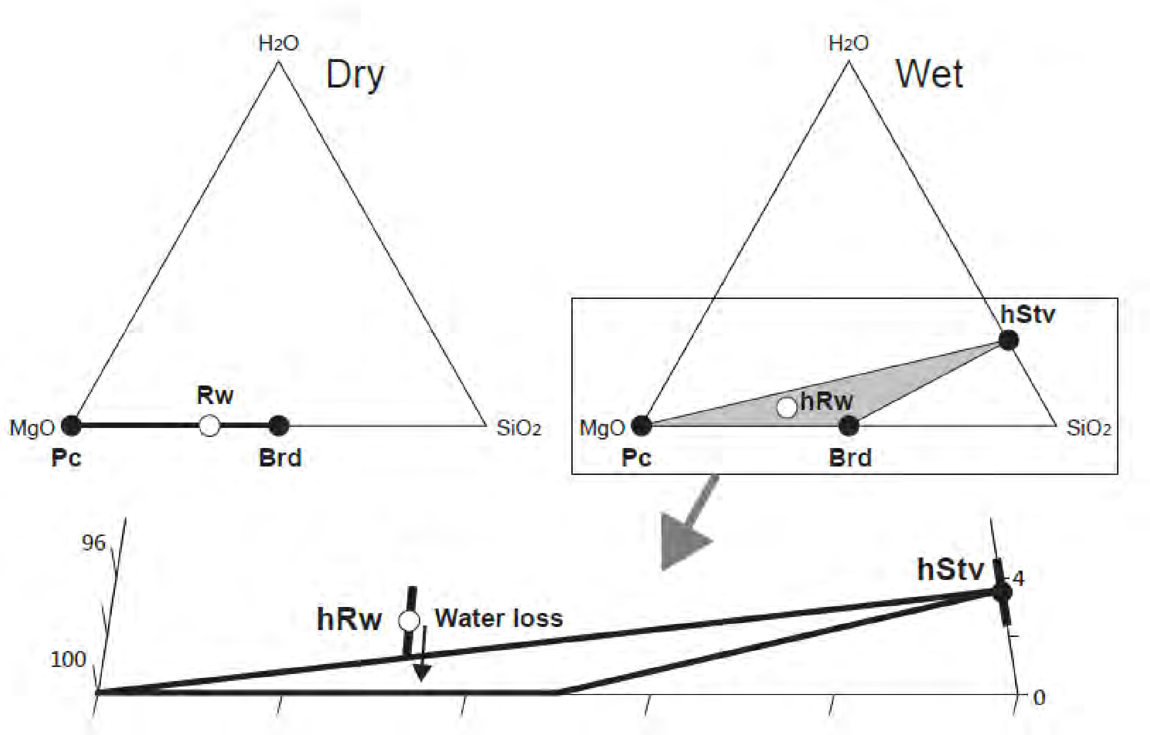

Fig. 3, The $MgO–SiO_2–H_2O$ ternary system and the formation of the lower-mantle minerals from anhydrous and hydrous Rw (left, Eq. 1, and right, Eq. 2). The H_2O contents in the top two ternary diagrams are exaggerated for the visibility of the expected phase assemblages. We present the properly scaled compositions of our starting material and recovered sample in the bottom diagram.

Previous studies have reported IR spectra of hydrous Stv (Spektor et al., 2016, 2011). However, these samples were synthesized at pressures lower than 10 GPa and therefore within the stability of Stv without a $CaCl_2$ type distortion. In contrast, our samples, all of which are synthesized above 35 GPa, may have experienced a transition from $CaCl_2$ type (mStv) to Stv during the decompression for the recovery. Therefore, comparison of our IR spectra to those of hydrous Stv from low-P experiments should be made with caution.

Nevertheless, three modes at approximately 2550, 2870, and 3250 cm^{-1} from our samples show good agreement in frequency with those reported for a hydrous Stv sample (Spektor et al., 2011), although the intensity distribution is different (Fig. 2b). Our IR spectra are measured on a much smaller area, and therefore significantly fewer grains in the samples, recovered from the LHDAC experiments, whereas the former study (Spektor et al., 2011) was conducted for much larger sample synthesized in a multi-anvil press. In fact, as shown in Fig. 2b, the intensity distribution varies among different samples in our experiments, while mode frequencies are consistent with each other within 50 cm^{-1}, indicating the OH mode intensities of our samples are sensitive to crystallographic orientations and therefore preferred orientation. Different synthesis pressure and the sample history, discussed above, may explain the small but noticeable shift of the trend in the c/a and unit-cell volume relationship and the small but systematically lower frequencies (by 30–100 cm^{-1}) of the major IR-active OH modes of our samples compared with hStv from low-P synthesis (Fig. 2a,b). We note that our IR spectra is different from Schmandt et al. (2014) in that they observed a broad IR O-H band related to melting product while our IR band shows three distinct peaks of hydrous stishovite similar to Spektor et al. (2016).

Discussions

It is of interest why free silica phase forms even under the MgO saturated system we studied (our starting material was hydrous Mg_2SiO_4 ringwoodite). First, we can consider solid-state reaction. From the Gibbs phase rule, $F = C - \Phi + 2$ (F is degrees of freedom, C is chemical components, and Φ is number of phases in a system), for an $MgO–SiO_2$ system with two independent components (MgO and SiO_2; $C = 2$) at a range of P and T ($F = 2$), the maximum number of phases should be two ($\Phi = 2$). This is the case for anhydrous Rw in $MgO–SiO_2$ and thus explains the following phase change in the lower mantle:

$$Mg_2SiO_4\ (Rw) = MgSiO_3\ (Brd) + MgO\ (Pc) \qquad (1)$$

In our experiments, Rw contained H_2O and therefore we should consider a ternary system, $MgO–SiO_2–H_2O$ ($C = 3$). In this case, the Gibbs rule predicts a ternary phase assemblage ($\Phi = 3$) at a range of P and T. We indeed observed the stability of the Brd + Pc + Stv (or mStv) ternary phase assemblage at pressures between 35 and 59 GPa. Some phases in our final products should contain H_2O and as shown above Stv (or mStv) plays such a role. As shown in Fig. 3, hydrous Stv (or mStv), together with Pc and Brd, can form a triangle in the ternary phase diagram for a stable phase assemblage. Because Brd is the phase with Si, in order to form hydrous Stv (or mStv), a partial breakdown is needed:

$$(Mg_{1-x}H_{2x})_2SiO_4\ (hRw) = (1 - x - y)MgSiO_3\ (Brd) + (1 - x + y)MgO\ (Pc) + ySiO_2 2xH_2O\ (hStv)\ (2)$$

where $2x$ is the amount of H_2O originally in Rw and y is the molar fraction of the Brd breakdown to Pc + Stv (or mStv). Hydrogen would mainly substitute Mg in ringwoodite (Smyth et al. 2004) while stishovite would store hydrogen through direct substitution (Spektor et al., 2011).

In Fig. 3, our starting composition is slightly above the triangle formed by the three lower-mantle phases after the transition. We note that the distance between the Rw composition and the phase assemblage triangle of Brd + Pc + Stv is within the estimated uncertainty of the H_2O content. The H_2O contents were estimated using different methods for Rw and Stv (IR and XRD, respectively) and therefore the systematic differences in these two methods may have contributed more than the estimated error presented in Fig. 3. The ternary phase diagram we presented here assumes that the system was closed with no interaction between Rw and the surrounding medium, either Ar or Ne. However, some amounts of H_2O could have been released to the pressure medium during heating. The noble gas medium escaped from the sample chamber during recovery, therefore we could not measure the amount of H_2O in the medium. If our hydrous Rw lost H_2O to the medium during the initial stage of laser heating, the composition point would shift toward the MgO–SiO_2 line, and possibly lied within the Brd–Pc–Stv triangle.

The hypothesis presented here can be further examined if the fractions of the phases can be reliably determined. We attempted Rietveld refinements (Fig. S5) to obtain phase fractions. However, we found that the intensities of the phases vary strongly at different spots in the sample, likely because of strong recrystallization during laser heating. Our 2D diffraction image in Fig. S4 shows that we only have a few single-crystal-like grains for the phases instead of randomly oriented powder which is required for successful Rietveld refinements. The observation explains the strong variation in the intensity. Because of the limitation, we could not reliably constrain the phase fractions through Rietveld refinements.

Second, we consider possibility of melt-involved process. A recent high-pressure experiment (Walter et al., 2015) observed Stv at lower-mantle related pressures in MgO–Al_2O_3–SiO_2–H_2O even when Mg/Si > 1, which is similar to our study. The study documented that Stv appeared at temperature above 1300 K and remained stable to at least 1900 K at 30 to 50 GPa together with Brd and MgO. They related the appearance of Stv to hydrous melting.

Although the H_2O content in Stv was not reported, the observation of Stv in the Mg-rich system in Walter et al. (2015) is consistent with our study and supports the important role of H_2O for the lower-mantle mineralogy. At lower temperatures, phase D and phase H were observed in the former study (Walter et al., 2015), which was not the case in our experiments. However, their samples contained a factor of 3–5 greater amounts of H_2O than our samples, which could change the phase behavior. The amount of H_2O in our experiments is more consistent with recent estimations for H_2O content in the mantle transition zone (Fei et al., 2017).

An experimental study of a $(Mg_{0.9}Fe_{0.1})_2SiO_4$ Rw sample with 1.1(1) wt% H_2O reported the observation of Brd, (Mg,Fe)O, and brucite after laser heating to 1873 K at 30 GPa (Schmandt et al., 2014). They identified small amorphous regions in the TEM analysis of the quenched samples and attributed them to hydrous melting.

If these former observations are applicable for our experiments, it can be hypothesized that generation of silica-rich hydrous melt and its subsequent cooling below melting temperature may crystallize dense silica in our experiment. However, in our in-situ experiments shown in Fig. S3, we did not find any sign of melting. For example, coupling behavior change is common across melting (Walter et al., 2015), which was not found in our study. In addition, our in-situ experiments show immediate appearance of silica from the hydrous ringwoodite starting material together with Brd and Pc. Such an observation is inconsistent with the melting-related precipitate possibility.

In Schmandt et al. (2014), the XRD pattern does not show any silica peaks and their reported IR spectra for OH are different from Stv. The melting temperature of silicates generally increases with pressure. Their pressure was lower than our experiments (Fig. 4). In addition, Fe in their Rw sample could reduce the melting temperature. Therefore, it is difficult to relate their results to our experimental observations.

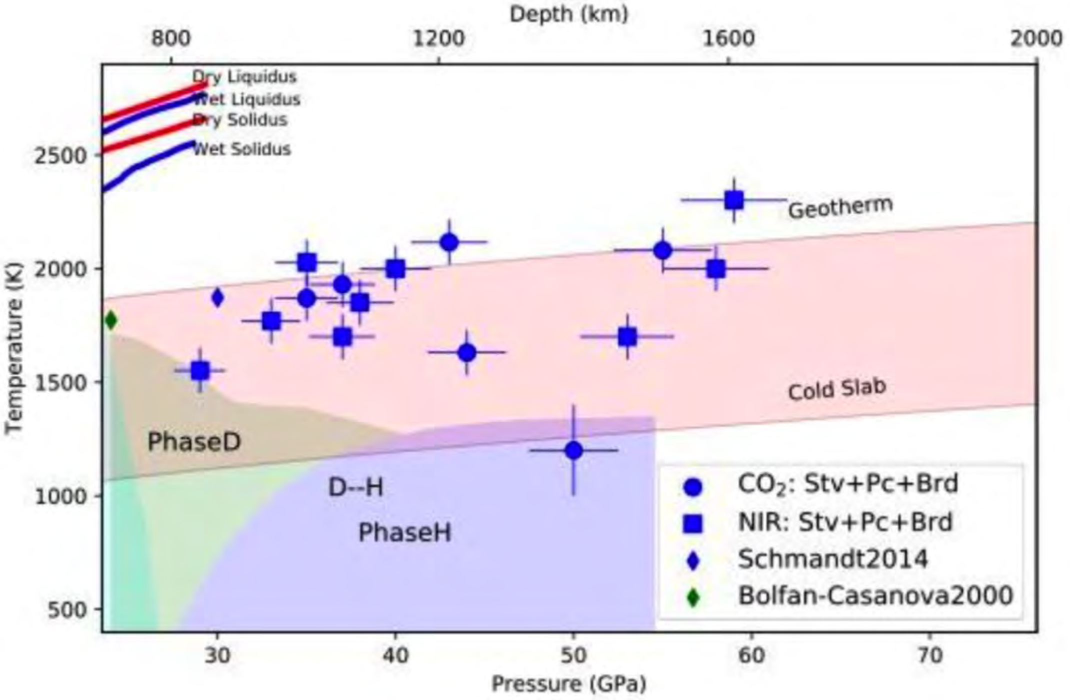

Fig. 4. Pressure and temperature conditions for the experimental runs with the observed phase assemblages. We plot the expected temperature ranges at different depths between the cold subducting slabs and the mantle geotherm (Brown and Shankland, 1981; Syracuse et al., 2010). We also show dry liquidus and solidus of the pyrolitic composition, wet liquidus and solidus of pyrolitic composition with 2 wt% water from Litasov and Ohtani (2002). The stability fields of phase D and phase H are from previous studies (Litasov and Ohtani, 2002; Nishi et al., 2014). CO_2: CO_2 laser-heating experiments, and NIR: NIR laser-heating experiments. We also plotted melting experiment performed by other studies (Bolfan-Casanova et al., 2000; Schmandt et al., 2014).

For a pyrolitic CaO–MgO–Al_2O_3–SiO_2, a multi-anvil press study showed that 2 wt% of H_2O, which is twice more than we have, reduces the melting temperature to 2400 K at 25 GPa (Litasov and Ohtani, 2002). Because it increases with pressure, the melting temperature should be higher than 2400 K at the pressure range of our experiments (Litasov and Ohtani, 2002). All of our experiments were conducted at temperatures below 2400 K, and we observed the formation of dense silica polymorph at temperatures as low as 1200–1630 K (Fig. S3). We also did not find any IR modes of brucite, which has been often related to melting in high-pressure samples (Schmandt et al., 2014). Therefore, the melting-involving possibility is less likely.

If stishovite observed in our experiments is related to partial melting, because we observed stishovite during in-situ heating, we can hypothesize that Brd undergoes incongruent melting and stishovite appears as a solidus phase, existing together with partial melt. However, such an observation has not been documented yet to our knowledge at the pressure range we studied.

Panero et al. (2003) documented that aluminous stishovite has an elevated amount of H_2O after partial melting in MORB composition. However, in this case, stishovite is already stable even in anhydrous MORB below melting temperature because of much higher concentration of SiO_2 in the composition. Therefore, unlike our case where stishovite cannot exist in anhydrous case because of the high Mg/Si ratio, the observation by Panero et al. (2003) is likely because of H_2O partitioning between partial melt and solid residue.

Saxena et al. (1996) reported breakdown of $MgSiO_3$ Brd to MgO and SiO_2 stishovite at pressures between 58 and 85 GPa. However, the later experiments have shown instead that $MgSiO_3$ Brd remains stable throughout the lower mantle (Serghiou et al., 1998; Shim et al., 2001b). The source of the earlier breakdown observation has been unclear. While it is intriguing to consider the effect of H_2O for the earlier experiments of breakdown from our new observations reported here, we also note that (Saxena et al., 1996) observed the stability of Brd at the pressure range we studied in this report.

From these considerations, our preferred interpretation of the silica formation in our experiments is the solid-solid reaction and stabilization of silica through H_2O storage in the phase. However, we believe future study is required for more firm conclusions particularly related to the possible partial melting origin of stishovite. For example, transmission electron microscopy (TEM) analysis would be helpful to further address the limitations in this study. Although we attempted, we found it difficult to recover the samples undergone extensive phase changes and recrystallization in a noble gas medium for TEM analysis. Therefore, technical development would be important to achieve the measurements. It is also of particular interest to explore the transition in mineralogy after the stability field of phase D at temperatures higher than the stability of phase H.

Implications

Numerous studies have documented Stv coexisting with (Mg,Fe)O and Brd (pyroxene with Brd-like composition) as inclusions in diamonds from the lower mantle (Kaminsky, 2012; Litvin et al., 2014; Stachel et al., 2005). As shown in Eq. 1, the coexistence of Stv is very difficult to explain in the anhydrous pyrolitic lower mantle. Diamond inclusions have been often related to fluids or H_2O (Kaminsky, 2012; Kohn et al., 2016; Tschauner et al., 2018). Here we showed that Stv (or mStv) could form a phase assemblage with Fp and Brd in an Mg-rich system if H_2O is present. Our observation, therefore, provides a new possible explanation for the coexistence of Stv with Fp and Brd in the lower-mantle diamonds. If so, those diamonds should originate from hydrous regions in the mid-mantle. We proposed that future studies measure the H_2O content of the Stv inclusions in lower-mantle diamonds. If future studies indeed support our interpretation for the stabilization of silica through H_2O storage in the lower mantle, such a change in mineralogy would impact our understanding on the H_2O cycle in Earth and other Earth-like planets in our solar system and extra-solar system.

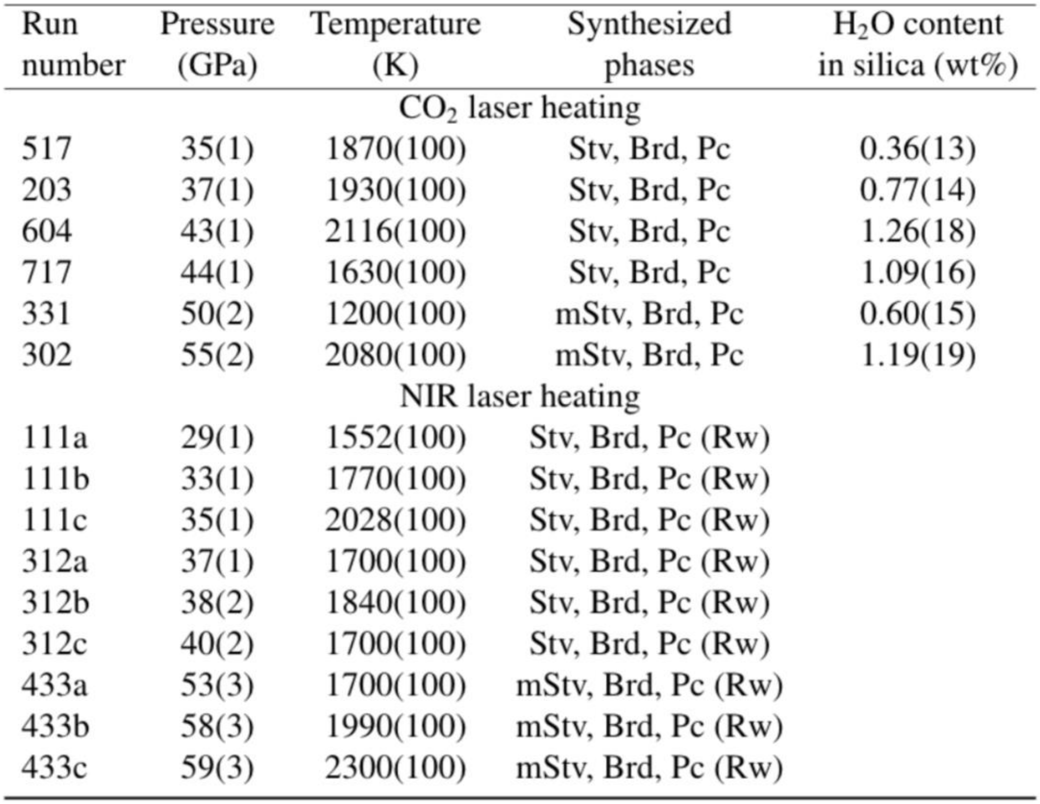

Run number	Pressure (GPa)	Temperature (K)	Synthesized phases	H_2O content in silica (wt%)
		CO_2 laser heating		
517	35(1)	1870(100)	Stv, Brd, Pc	0.36(13)
203	37(1)	1930(100)	Stv, Brd, Pc	0.77(14)
604	43(1)	2116(100)	Stv, Brd, Pc	1.26(18)
717	44(1)	1630(100)	Stv, Brd, Pc	1.09(16)
331	50(2)	1200(100)	mStv, Brd, Pc	0.60(15)
302	55(2)	2080(100)	mStv, Brd, Pc	1.19(19)
		NIR laser heating		
111a	29(1)	1552(100)	Stv, Brd, Pc (Rw)	
111b	33(1)	1770(100)	Stv, Brd, Pc (Rw)	
111c	35(1)	2028(100)	Stv, Brd, Pc (Rw)	
312a	37(1)	1700(100)	Stv, Brd, Pc (Rw)	
312b	38(2)	1840(100)	Stv, Brd, Pc (Rw)	
312c	40(2)	1700(100)	Stv, Brd, Pc (Rw)	
433a	53(3)	1700(100)	mStv, Brd, Pc (Rw)	
433b	58(3)	1990(100)	mStv, Brd, Pc (Rw)	
433c	59(3)	2300(100)	mStv, Brd, Pc (Rw)	

Tab. 1. Conditions and run products of the high-pressure experiments. The numbers in parentheses are the 1σ uncertainties. As discussed in the main text, it is difficult to resolve peaks from the orthorhombic modification ($CaCl_2$ type) of Stv (therefore mStv) because of the peak overlaps with Brd and Fp. For the case we have clear evidence for the orthorhombic modification at high pressure, we noted them as "mStv" in this table. Even in this case, mStv converts to Stv (tetragonal) during decompression. For the case we note as "Stv", although the diffraction patterns can be well indexed with Stv, we do not rule out the possibility of mStv, because of subtle differences in diffraction patterns between Stv and mStv.

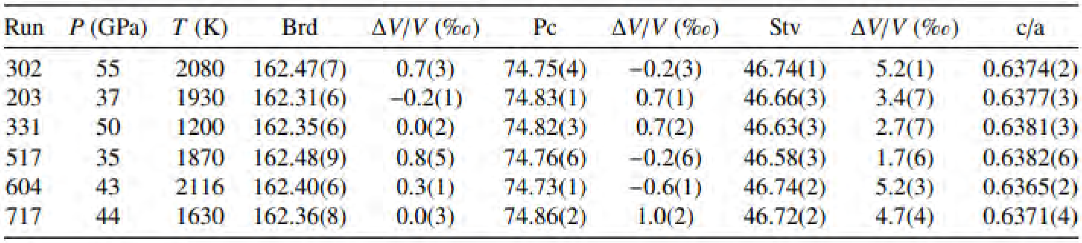

Run	P (GPa)	T (K)	Brd	$\Delta V/V$ (‰)	Pc	$\Delta V/V$ (‰)	Stv	$\Delta V/V$ (‰)	c/a
302	55	2080	162.47(7)	0.7(3)	74.75(4)	−0.2(3)	46.74(1)	5.2(1)	0.6374(2)
203	37	1930	162.31(6)	−0.2(1)	74.83(1)	0.7(1)	46.66(3)	3.4(7)	0.6377(3)
331	50	1200	162.35(6)	0.0(2)	74.82(3)	0.7(2)	46.63(3)	2.7(7)	0.6381(3)
517	35	1870	162.48(9)	0.8(5)	74.76(6)	−0.2(6)	46.58(3)	1.7(6)	0.6382(6)
604	43	2116	162.40(6)	0.3(1)	74.73(1)	−0.6(1)	46.74(2)	5.2(3)	0.6365(2)
717	44	1630	162.36(8)	0.0(3)	74.86(2)	1.0(2)	46.72(2)	4.7(4)	0.6371(4)

Tab. 2. The unit cell volumes of bridgmanite (Brd), periclase (MgO) and stishovite (Stv) measured at 1 bar after pressure and temperature quench. The values were obtained through Rietveld refinements (see an example in Fig. S5). The unit-cell parameters of Brd, Pc, and Stv are compared with those reported for pure $MgSiO_3$ (162.349Å^3) (Ross et al. 1990), MgO (74.778Å^3) (Dorogokupets et al. 2007), and anhydrous Stv (46.502Å^3) (Andrault et al. 2003), respectively, at 1 bar. The *c/a* ratio for stishovite were also included in the table.

Acknowledgments

This work was supported by NSF grants (EAR1321976 and EAR1401270) and NASA grant (80NSSC18K0353) to S.H.S. H.C. has been supported by the Keck foundation (PI: P. Buseck). The results reported herein benefit from collaborations and/or information exchange within NASA's Nexus for Exoplanet System Science (NExSS) research coordination network sponsored by NASA's Science Mission Directorate. We acknowledge the use of facilities within the Eyring Materials Center at Arizona State University. The synchrotron experiments were conducted at GSECARS, Advanced Photon Source (APS), Advanced Light Source (ALS), and National Synchrotron Light

Source (NSLS). GSECARS is supported by NSF-Earth Science (EAR-1128799) and DOE-GeoScience (DE-FG02-94ER14466). The Multi-Anvil Cell Assembly Project, DAC gas loading, and the U2A beamline at the NSLS are supported by COMPRES under NSF EAR 11-43050. APS, ALS, and NSLS are supported by DOE, under contracts DE-AC02-06CH11357, DE-AC02-05CH11231, and DE-SC0012704, respectively. The experimental data for this paper are available by contacting SHDShim@asu.edu or hchen156@asu.edu.

References cited

Andrault, D., Angel, R. J., Mosenfelder, J. L. & Bihan, T. L. (2003) Equation of state of stishovite to lower mantle pressures. American Mineralogist 88, 301–307.

Bolfan-Casanova, N., Keppler, H., and Rubie, D.C. (2000) Water partitioning between nominally anhydrous minerals in the MgO–SiO2–H2O system up to 24 GPa: implications for the distribution of water in the Earth's mantle. Earth and Planetary Science Letters, 182, 209–221.

Bolfan‐Casanova, N., Mackwell, S., Keppler, H., McCammon, C., and Rubie, D.C. (2002) Pressure dependence of H solubility in magnesiowüstite up to 25 GPa: Implications for the storage of water in the Earth's lower mantle. Geophysical Research Letters, 29, 89-1-89–4.

Bolfan‐Casanova, N., Keppler, H., and Rubie, D.C. (2003) Water partitioning at 660 km depth and evidence for very low water solubility in magnesium silicate perovskite. Geophysical Research Letters, 30.

Brown, J.M., and Shankland, T.J. (1981) Thermodynamic parameters in the Earth as determined from seismic profiles. Geophysical Journal International, 66, 579–596.

Dorogokupets, P. & Dewaele, A.(2007) Equations of state of MgO, Au, Pt, NaCl-B1, and NaCl- B2: Internally consistent high-temperature pressure scales. High Pressure Research 27, 431–446 .

Fei, H., Yamazaki, D., Sakurai, M., Miyajima, N., Ohfuji, H., Katsura, T., and Yamamoto, T. (2017) A nearly water-saturated mantle transition zone inferred from mineral viscosity. Science Advances, 3, e1603024.

Fei, Y., Wang, Y., and Finger, L.W. (1996) Maximum solubility of FeO in (Mg, Fe)SiO $_3$ -perovskite as a function of temperature at 26 GPa: Implication for FeO content in the lower mantle. Journal of Geophysical Research: Solid Earth, 101, 11525–11530.

Hirose, K., Takafuji, N., Sata, N., and Ohishi, Y. (2005) Phase transition and density of subducted MORB crust in the lower mantle. Earth and Planetary Science Letters, 237, 239–251.

Hirschmann, M.M. (2006) Water, Melting, and the Deep Earth H2o Cycle. Annual Review of Earth and Planetary Sciences, 34, 629–653.

Kaminsky, F. (2012) Mineralogy of the lower mantle: A review of 'super-deep' mineral inclusions in diamond. Earth-Science Reviews, 110, 127–147.

Kesson, S.E., Fitz Gerald, J.D., and Shelley, J.M. (1998) Mineralogy and dynamics of a pyrolite lower mantle. Nature, 393, 252–255.

Kohn, S.C., Speich, L., Smith, C.B., and Bulanova, G.P. (2016) FTIR thermochronometry of natural diamonds: A closer look. Lithos, 265, 148–158.

Kunz, M., MacDowell, A.A., Caldwell, W.A., Cambie, D., Celestre, R.S., Domning, E.E., Duarte, R.M., Gleason, A.E., Glossinger, J.M., Kelez, N., and others (2005) A beamline for high-pressure studies at the Advanced Light Source with a superconducting bending magnet as the source. Journal of Synchrotron Radiation, 12, 650–658.

Kurnosov, A., Marquardt, H., Frost, D.J., Ballaran, T.B., and Ziberna, L. (2017) Evidence for a Fe3+-rich pyrolitic lower mantle from (Al,Fe)-bearing bridgmanite elasticity data. Nature, 543, 543–546.

Lakshtanov, D.L., Sinogeikin, S.V., Litasov, K.D., Prakapenka, V.B., Hellwig, H., Wang, J., Sanches-Valle, C., Perrillat, J.-P., Chen, B., Somayazulu, M., and others (2007) The post-stishovite phase transition in hydrous alumina-bearing SiO2 in the lower mantle of the earth. Proceedings of the National Academy of Sciences, 104, 13588–13590.

Lee, K.K.M., O'Neill, B., Panero, W.R., Shim, S.-H., Benedetti, L.R., and Jeanloz, R. (2004) Equations of state of the high-pressure phases of a natural peridotite and implications for the Earth's lower mantle. Earth and Planetary Science Letters, 223, 381–393.

Leinenweber, K.D., Tyburczy, J.A., Sharp, T.G., Soignard, E., Diedrich, T., Petuskey, W.B., Wang, Y., and Mosenfelder, J.L. (2012) Cell assemblies for reproducible multi-anvil experiments (the COMPRES assemblies). American Mineralogist, 97, 353–368.

Litasov, K., and Ohtani, E. (2002) Phase relations and melt compositions in CMAS–pyrolite–H2O system up to 25 GPa. Physics of the Earth and Planetary Interiors, 134, 105–127.

Litvin, Y., Spivak, A., Solopova, N., and Dubrovinsky, L. (2014) On origin of lower-mantle diamonds and their primary inclusions. Physics of the Earth and Planetary Interiors, 228, 176–185.

Mao, H.K., Bell, P.M., Shaner, J.W., and Steinberg, D.J. (1978) Specific volume measurements of Cu, Mo, Pd, and Ag and calibration of the ruby R1 fluorescence pressure gauge from 0.06 to 1 Mbar. Journal of Applied Physics, 49, 3276–3283.

McDonough, W.F., and Sun, S. -s. (1995) The composition of the Earth. Chemical Geology, 120, 223–253.

Newville, M., Stensitzki, Till., Allen, D. B., and Ingargiola, A. (2014) LMFIT: Non-Linear Least-Square Minimization and Curve-Fitting for Python. Zenodo, 10.5281/zenodo.11813

Nishi, M., Irifune, T., Tsuchiya, J., Tange, Y., Nishihara, Y., Fujino, K., and Higo, Y. (2014) Stability of hydrous silicate at high pressures and water transport to the deep lower mantle. Nature Geoscience, 7, 224–227.

Nisr, C., Shim, S.-H., Leinenweber, K., and Chizmeshya, A. (2017a) Raman spectroscopy of water-rich stishovite and dense high-pressure silica up to 55 GPa. American Mineralogist, 102, 2180–2189.

Nisr, C., Leinenweber, K., Prakapenka, V., Prescher, C., Tkachev, S., and Shim, S.-H. (2017b) Phase transition and equation of state of dense hydrous silica up to 63 GPa. Journal of Geophysical Research, 122,2017JB014055.

Panero, W.R., Pigott, J.S., Reaman, D.M., Kabbes, J.E., and Liu, Z. (2015) Dry (Mg,Fe)SiO3 perovskite in the Earth's lower mantle. Journal of Geophysical Research: Solid Earth, 120, 2014JB011397.

Pearson, D.G., Brenker, F.E., Nestola, F., McNeill, J., Nasdala, L., Hutchison, M.T., Matveev, S., Mather, K., Silversmit, G., Schmitz, S., and others (2014) Hydrous mantle transition zone indicated by ringwoodite included within diamond. Nature, 507, 221–224.

Prakapenka, V.B., Kubo, A., Kuznetsov, A., Laskin, A., Shkurikhin, O., Dera, P., Rivers, M.L., and Sutton, S.R. (2008) Advanced flat top laser heating system for high pressure research at GSECARS: application to the melting behavior of germanium. High Pressure Research, 28, 225–235.

Prescher, C., and Prakapenka, V.B. (2015) DIOPTAS: a program for reduction of two-dimensional X-ray diffraction data and data exploration. High Pressure Research, 35, 223–230.

Rivers, M., Prakapenka, V.B., Kubo, A., Pullins, C., Holl, C.M., and Jacobsen, S.D. (2008) The COMPRES/GSECARS gas-loading system for diamond anvil cells at the Advanced Photon Source. High Pressure Research, 28, 273–292.

Ross, M., Mao, H.K., Bell, P.M., and Xu, J.A. (1986) The equation of state of dense argon: A comparison of shock and static studies. The Journal of Chemical Physics, 85, 1028–1033.

Ross, N. L. & Hazen, R. M.(1990) High-pressure crystal chemistry of MgSiO3 perovskite. Physics and Chemistry of Minerals 17, 228–237.

Rossman, G.R. (1996) Studies of OH in nominally anhydrous minerals. Physics and Chemistry of Minerals, 23, 299–304.

Saxena, S.K., Dubrovinsky, L.S., Lazor, P., Cerenius, Y., Häggkvist, P., Hanfland, M., and Hu, J. (1996) Stability of Perovskite (MgSiO3) in the Earth's Mantle. Science, 274, 1357–1359.

Schmandt, B., Jacobsen, S.D., Becker, T.W., Liu, Z., and Dueker, K.G. (2014) Dehydration melting at the top of the lower mantle. Science, 344, 1265–1268.

Serghiou, G., Zerr, A., and Boehler, R. (1998) (Mg,Fe)SiO3-Perovskite Stability Under Lower Mantle Conditions. Science, 280, 2093–2095.

Shim, S.-H., Duffy, T.S., and Shen, G. (2001a) Stability and Structure of MgSiO3 Perovskite to 2300-Kilometer Depth in Earth's Mantle. Science, 293, 2437–2440.

——— (2001b) The post-spinel transformation in Mg2SiO4 and its relation to the 660-km seismic discontinuity. Nature, 411, 571–574.

Shim, S.-H., Grocholski, B., Ye, Y., Alp, E.E., Xu, S., Morgan, D., Meng, Y., and Prakapenka, V.B. (2017) Stability of ferrous-iron-rich bridgmanite under reducing midmantle conditions. Proceedings of the National Academy of Sciences, 114, 6468–6473.

Smyth, J.R. (1994) A crystallographic model for hydrous wadsleyite (β-Mg2SiO4): An ocean in the Earth's interior? American Mineralogist, 79, 1021–1024.

Smyth, J.R., Holl, C.M., Frost, D.J., Jacobsen, S.D. Langenhorst, F and Mccammon CA(2003) Structural systematics of hydrous ringwoodite and water in Earth's interior. American Mineralogist, 88, 1402–1407.

Smyth, J.R., Holl, C.M., Frost, D.J., and Jacobsen, S.D. (2004) High pressure crystal chemistry of hydrous ringwoodite and water in the Earth's interior. Physics of the Earth and Planetary Interiors, 143, 271–278.

Spektor, K., Nylen, J., Stoyanov, E., Navrotsky, A., Hervig, R.L., Leinenweber, K., Holland, G.P., and Häussermann, U. (2011) Ultrahydrous stishovite from high-pressure hydrothermal treatment of SiO2. Proceedings of the National Academy of Sciences, 108, 20918–20922.

Spektor, K., Nylen, J., Mathew, R., Edén, M., Stoyanov, E., Navrotsky, A., Leinenweber, K., and Häussermann, U. (2016) Formation of hydrous stishovite from coesite in high-pressure hydrothermal environments. American Mineralogist, 101, 2514–2524.

Stachel, T., Brey, G.P., and Harris, J.W. (2005) Inclusions in Sublithospheric Diamonds: Glimpses of Deep Earth. Elements, 1, 73–78.

Syracuse, E.M., van Keken, P.E., and Abers, G.A. (2010) The global range of subduction zone thermal models. Physics of the Earth and Planetary Interiors, 183, 73–90.

Toby, B.H., and Von Dreele, R.B. (2013) *GSAS-II* : the genesis of a modern open-source all purpose crystallography software package. Journal of Applied Crystallography, 46, 544–549.

Tschauner, O., Huang, S., Greenberg, E., Prakapenka, V.B., Ma, C., Rossman, G.R., Shen, A.H., Zhang, D., Newville, M., Lanzirotti, A., and others (2018) Ice-VII inclusions in diamonds: Evidence for aqueous fluid in Earth's deep mantle. Science, 359, 1136–1139.

Walter, M.J., Thomson, A.R., Wang, W., Lord, O.T., Ross, J., McMahon, S.C., Baron, M.A., Melekhova, E., Kleppe, A.K., and Kohn, S.C. (2015) The stability of hydrous silicates in Earth's lower mantle: Experimental constraints from the systems MgO–SiO2–H2O and MgO–Al2O3–SiO2–H2O. Chemical Geology, 418, 16–29.

Ye, Y., Prakapenka, V., Meng, Y., and Shim, S.-H. (2017) Inter-comparison of the Gold, Platinum, and MgO Pressure Scales up to 140 GPa and 2,500 K. Journal of Geophysical Research: Solid Earth, 2016JB013811.

Figure captions

Fig. 1. X-ray diffraction patterns of lower-mantle minerals transformed from hydrous ringwoodite. a, 50 GPa after heating at 1200 K. b, 1 bar after recovery (X-ray wavelength of 0.3344 Å). The colored ticks below the patterns indicate the expected peak positions (Brd: bridgmanite, Pc: periclase (MgO), Stv: stishovite, Ct-SiO_2: $CaCl_2$-type silica (or mStv), Ar: argon, : hcp-Ar). The blue arrows highlight the peaks from Stv (or converted from mStv). The Miller indices are provided for the lines with significant intensities (10%).

Fig. 2. The solubility of H_2O in Stv (or mStv) and its effects on the lower-mantle mineralogy. a, The *c*/*a* ratio and the unit-cell volume of the recovered Stv co-existing with Brd and MgO. For comparison, we plot the data for hydrous Stv (Spektor et al., 2016). b, The IR spectra of the samples recovered from the CO_2 heating experiments (dots) with spectral fitting results (black curves). We also present the IR spectra of the starting material (hydrous Rw) and hydrous Stv (Spektor et al., 2011). The gap at 2800–3000 cm^{-1} is a region for C-H modes from CH contaminants on diamond anvils. After opening the diamond-anvil cell, we measured IR through one diamond anvil to prevent accidental loss of the sample.

Fig. 3, The $MgO–SiO_2–H_2O$ ternary system and the formation of the lower-mantle minerals from anhydrous and hydrous Rw (left, Eq. 1, and right, Eq. 2). The H_2O contents in the top two ternary diagrams are exaggerated for the visibility of the expected phase assemblages. We present the properly scaled compositions of our starting material and recovered sample in the bottom diagram.

Fig. 4. Pressure and temperature conditions for the experimental runs with the observed phase assemblages. We plot the expected temperature ranges at different depths between the cold subducting slabs and the mantle geotherm (Brown and Shankland, 1981; Syracuse et al., 2010). We also show dry liquidus and solidus of the pyrolitic composition, wet liquidus and solidus of pyrolitic composition with 2 wt% water from Litasov and Ohtani (2002). The stability fields of phase D and phase H are from previous studies (Litasov and Ohtani, 2002; Nishi et al., 2014). CO_2: CO_2 laser-heating experiments, and NIR: NIR laser-heating experiments. We also plotted melting experiment performed by other studies (Bolfan-Casanova et al., 2000; Schmandt et al., 2014).